Journal of Power Sources 267 (2014) 227–234

Contents lists available at ScienceDirect

Journal of Power Sources

journal homepage: www.elsevier.com/locate/jpowsour

Short communication

Synthesis and performances of $2LiFePO_4 \cdot Li_3V_2(PO_4)_3/C$ cathode materials via spray drying method with double carbon sources

Jia-feng Zhang, Chao Shen, Bao Zhang*, Jun-chao Zheng*, Chun-li Peng, Xiao-wei Wang, Xin-bo Yuan, Hui Li, Guo-min Chen

School of Metallurgy and Environment, Central South University, Changsha 410083, PR China

HIGHLIGHTS

- Spherical $2LiFePO_4 \cdot Li_3V_2(PO_4)_3/C$ composite was synthesized via spray-drying process.
- The raw materials are $Fe_4(VO_4)_4 \cdot 5H_2O$, LiH_2PO_4, glucose and oxalic acid.
- $2LiFePO_4 \cdot Li_3V_2(PO_4)_3/C$ composite has a high tap density of 1.66 g cm^{-3}.
- $2LiFePO_4 \cdot Li_3V_2(PO_4)_3/C$ composite shows excellent capacity and rate performance.

ARTICLE INFO

Article history:
Received 4 January 2014
Received in revised form
12 April 2014
Accepted 30 April 2014
Available online 14 May 2014

Keywords:
Lithium ion battery
$Fe_4(VO_4)_4 \cdot 5H_2O$
Ultrasonic-aided precipitation
$2LiFePO_4 \cdot Li_3V_2(PO_4)_3/C$
Spray drying

ABSTRACT

The $2LiFePO_4 \cdot Li_3V_2(PO_4)_3/C$ samples are synthesized through spray drying method. Glucose and oxalic acid are used as collaborative carbon sources to improve the electrochemical performance of $2LiFePO_4 \cdot Li_3V_2(PO_4)_3/C$ composites. XRD results reveal the $LiFePO_4 \cdot Li_3V_2(PO_4)_3/C$ samples are composed of orthorhombic $LiFePO_4$ and monoclinic $Li_3V_2(PO_4)_3$ phases. SEM results reveal that the nano-spherical $Fe_4(VO_4)_4 \cdot 5H_2O$ are about 80 nm and the $2LiFePO_4 \cdot Li_3V_2(PO_4)_3/C$ composites possess a micro-nano spherical morphology with carbon coating layer. The samples show the best electrochemical performance when the mass ration of glucose and oxalic is 6:4, it can deliver a capacity of 147.6 mAh g^{-1}, 145.0 mAh g^{-1}, 134.1 mAh g^{-1} and 123.0 mAh g^{-1} at the rates of 0.1C, 1C, 5C and 10C, respectively.

1. Introduction

Olivine-type $LiFePO_4$ is one of the most promising cathode materials for its high power density, stable structure, safety and abundant resources [1]. However, $LiFePO_4$ has inherently poor electrical conductivity (1.8×10^{-9} S cm^{-1}) and ionic conductivity (10^{-16}–10^{-14} S cm^{-1}), which hinder its wide applications [2,3]. Compared with $LiFePO_4$, the NASCION structure $Li_3V_2(PO_4)_3$ possesses superior electrical conductivity (2.4×10^{-7} S cm^{-1}) and ionic conductivity (10^{-9}–10^{-8} S cm^{-1}),which enables Li ions to intercalate and deintercalate effortlessly [4–6]. Besides, cations (Fe^{2+} and V^{3+}) mutual doping could increase the conductivity of the materials aid to the grain boundary, phase boundary and crystal defects [11,25–27].Therefore, there may be a possibility for the improvement of ionic diffusivity for $LiFePO_4$ by incorporating of $Li_3V_2(PO_4)_3$. Besides, the theoretic specific capacity of $Li_3V_2(PO_4)_3$ is 197 mAh g^{-1},which is higher than that of $LiFePO_4$ (170 mAh g^{-1}). Hence, it is a novel strategy for enhancing the electrochemical performance of $LiFePO_4$ by synthesizing the $xLiFePO_4 \cdot yLi_3V_2(PO_4)_3$ composites [7–24].

So far, a series of $xLiFePO_4 \cdot yLi_3V_2(PO_4)_3$ composites have been extensively investigated. The results confirm that the $Li_3V_2(PO_4)_3$ can apparently improve the electrochemical properties of $LiFePO_4$ [7–19]. To further improve the high-rate capacity and cycling stability of $xLiFePO_4 \cdot yLi_3V_2(PO_4)_3$ composites, the nanopartilces with a thin carbon coating layer is an effective way is to accelerate the diffusion of lithium-ions and electronic conductivity [7–26]. At the same time, considering the practical energy density, micron-nano spherical particles combined the high specific capacity and enhanced kinetics of nano-sized building blocks can be a good choice to optimize the material properties [28–30].

* Corresponding authors. Tel.: +86 731 88836357.
E-mail addresses: csuzjf@vip.163.com, csuzjf@163.com (B. Zhang), jczheng@csu.edu.cn (J.-c. Zheng).

http://dx.doi.org/10.1016/j.jpowsour.2014.04.153
0378-7753/

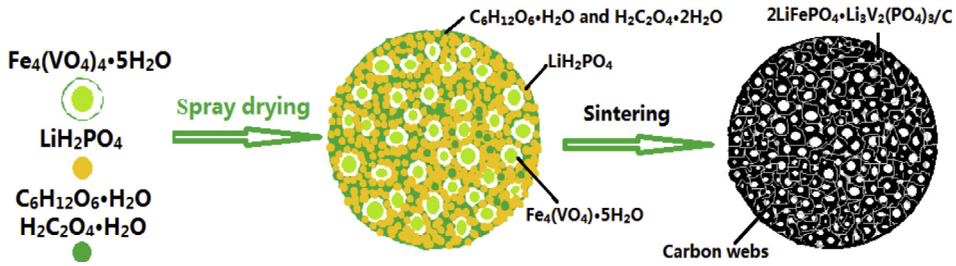

Fig. 1. Schematic illustration of the preparation process and microstructure characteristic the $2LiFePO_4 \cdot Li_3V_2(PO_4)_3/C$ composites.

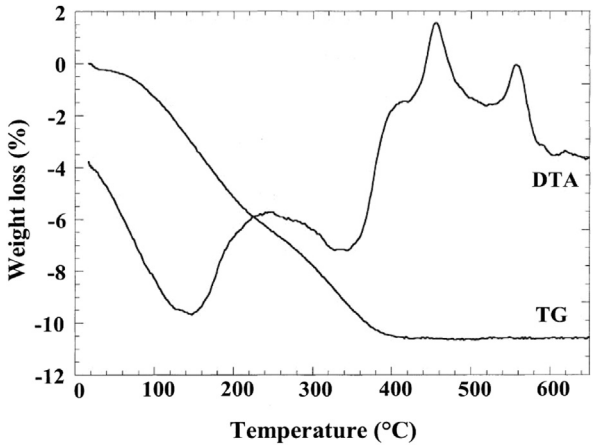

Fig. 2. TG-DTA curves of $Fe_4(VO_4)_4 \cdot xH_2O$ precursor.

It has been reported that coating conductive carbon onto the surface of $LiFePO_4$, $Li_3V_2(PO_4)_3$ and $xLiFePO_4 \cdot yLi_3V_2(PO_4)_3$ particles is an effective method for updating the electrochemical performance [10–23]. To our best knowledge, the surface carbon depends significantly on carbon source. Up to now various carbon sources have been employed for carbon-coating in $LiFePO_4$ and $Li_3V_2(PO_4)_3$ samples, such as glucose [8,26,31,32], oxalic acid [13,15,18,33], sucrose [23,24,34], polyvinyl alcohol [35,36], polyethylene glycol [37], citric acid [11,20,22,25], etc. Double carbon sources have been recently applied to improve the quality of carbon coating in $LiFePO_4$ and $Li_3V_2(PO_4)_3$ to achieve excessive electronic conductivity and lithium transfer [38,39].

In this work, the precursor $Fe_4(VO_4)_4 \cdot 5H_2O$ with uniformly distributed Fe and V was obtained via ultrasonic-aided precipitation route. Micro-nano spherical $2LiFePO_4 \cdot Li_3V_2(PO_4)_3/C$ samples were prepared by spray drying method. Glucose and oxalic acid were chosen as double carbon sources. The effect of mass ratio about glucose and oxalic acid on the electrochemical performance has been investigated.

2. Experimental

2.1. Preparation

$Fe_4(VO_4)_4 \cdot xH_2O$ was prepared by ultrasonic-aided precipitation method. First, 20.5 g of $Fe(NO_3)_3 \cdot 9H_2O$ and 5.9 g of NH_4VO_3 were dissolved in 1 L deionized water. Second, the mixture was transferred into an ultrasonic-aided reaction vessel under vigorous stirring at room temperature. Meanwhile, $NH_3 \cdot H_2O$ was employed to adjust the pH of the solution to 6. Then, a yellow precipitate $Fe_4(VO_4)_4 \cdot xH_2O$ was obtained. Finally, the precipitate was collected and dried in an oven at 60 °C.

The reaction may occur as follows:

$$V_4O_{12}^{4-} + 4Fe^{3+} + 8OH^- + nH_2O \rightarrow Fe_4(VO_4)_4 \cdot xH_2O \quad (1)$$

The $2LiFePO_4 \cdot Li_3V_2(PO_4)_3/C$ composites were synthesized via spray drying method. Originally, as-prepared $Fe_4(VO_4)_4 \cdot xH_2O$ and commercial LiH_2PO_4(10.4 g) were mixed with different proportion for glucose and oxalic acid in deionized water. Then, the mixture was ball milled in a planetary mill and dried in a spray-dryer by hot air. The as-obtained powders were sintered in a horizontal quartz tube at 700 °C for 12 h with Ar atmosphere. Finally, the $2LiFePO_4 \cdot Li_3V_2(PO_4)_3/C$ composites were obtained. Fig. 1 shows the relationship between the preparation process and microstructure characteristics of the $2LiFePO_4 \cdot Li_3V_2(PO_4)_3/C$ composites. The samples synthesized with the mass ratio of glucose to oxalic acid of 2:8(actual addition is 10 g:40 g), 6:4(actual addition is 30 g:20 g)

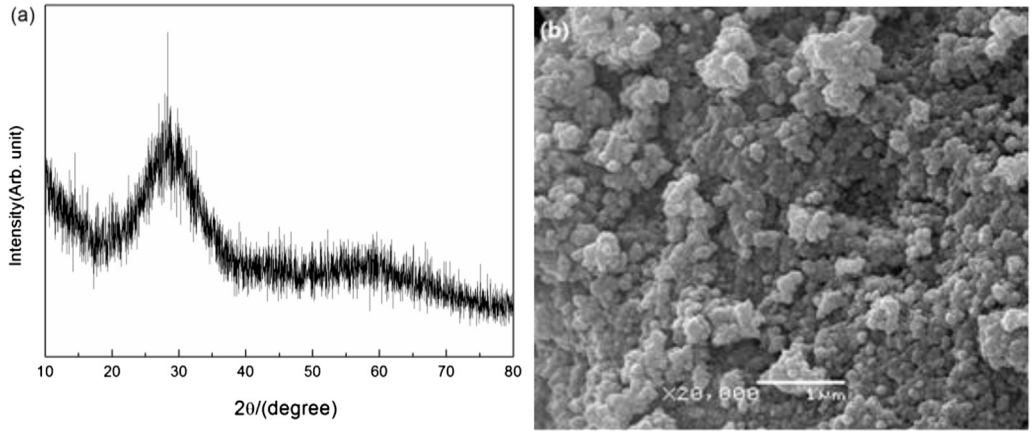

Fig. 3. XRD pattern (a) and SEM image (b) of $Fe_4(VO_4)_4 \cdot 5H_2O$ precursor.

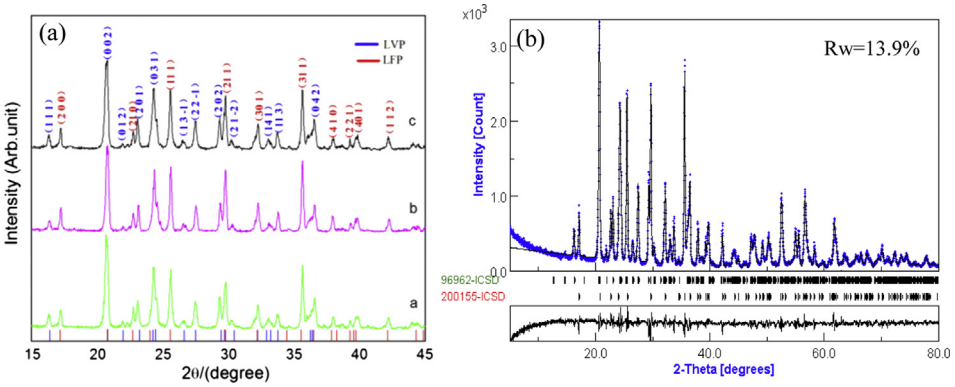

Fig. 4. XRD patterns (a) of (a)2LFP·LVP-S28; (b)2LFP·LVP-S64; (c) 2LFP·LVP-S82 and Rietveld refinement result (b) for 2LFP·LVP-S64.

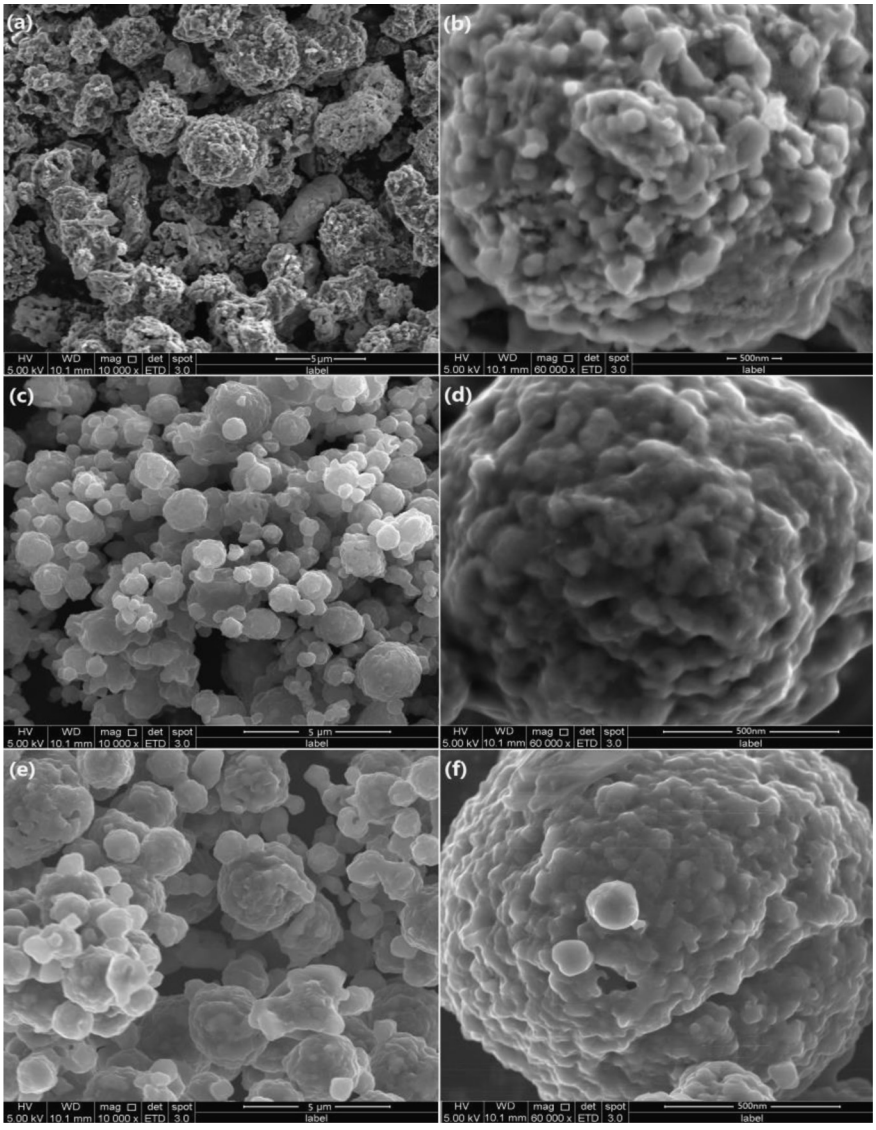

Fig. 5. SEM images of (a) (b) 2LFP·LVP-S28; (c) (d) 2LFP·LVP-S64; (e) (f) 2LFP·LVP-S82.

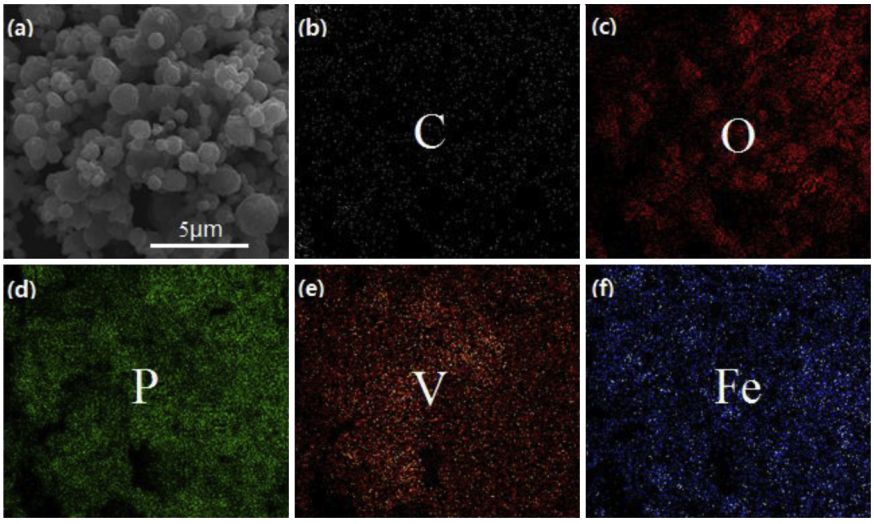

Fig. 6. SEM images of (a) 2LFP·LVP-S64 and elemental mapping for (b) C, (c) O, (d) P, (e) V, (f) Fe.

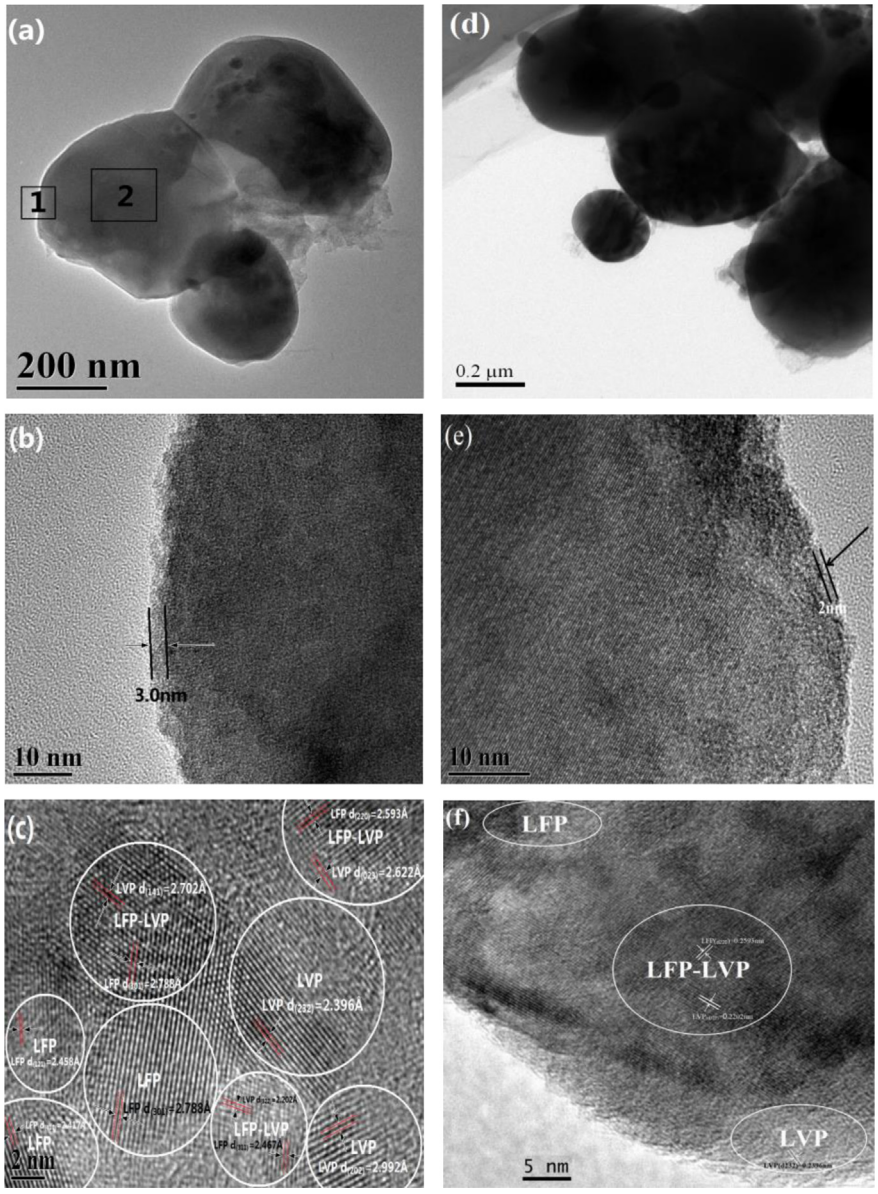

Fig. 7. The TEM image of (a) 2LFP·LVP-S64 particles, the HRTEM image of (b) selected region 1, (c) selected region 2 and (d) 2LFP·LVP-S28 particles, the HRTEM image (b) and (c).

and 8:2(actual addition is 40 g:10 g) are named 2LFP·LVP-S28, 2LFP·LVP-S64 and 2LFP·LVP-S82, respectively.

2.2. Characterization

The mole ratio Fe/V of as-prepared $Fe_4(VO_4)_4 \cdot xH_2O$ was determined by chemical titration. Furthermore, the TG and DTA synchronous tester was used (shimadzu DTG-60H) to confirm the composition of $Fe_4(VO_4)_4 \cdot xH_2O$. Meanwhile, X-ray diffraction (XRD, Rigaka D/MAX 2500 V) with CuKα radiation (Kα = 0.154 nm) was employed to identify the crystalline structures of the materials. The surface morphologies and particle information of the samples were observed by scanning electron microscopy (SEM) system (JSM-6380LV) and transmission electron microscopy (TEM) (Hitachi, H-8100).

Electrochemical characterizations were performed using a CR2025 coin-type cell. For the positive electrode fabrication, the prepared powders (80 wt%) were mixed with carbon black (10 wt%) and polyvinylidene fluoride (10 wt%) in N-methylpyrrolidone to form a homogeneous slurry, then which was spread uniformly on an aluminum foil and dried in a vacuum oven at 120 °C. In contrast, the negative electrode was a lithium-metal foil that also acted as a reference electrode. Then, a porous membrane (Celgard 2300) was used as a separator; and the electrolyte was 1 mol L^{-1} $LiPF_6$ dissolved in a mixture of ethylene carbonate, dimethyl carbonate, and methyl-ethyl carbonate with a volume ratio of 1:1:1. In addition, the coin cells were charged at 0.1C rate and discharged at the rates of 0.1C, 1C, 5C and 10C over the voltage range of 2.5 V–4.5 V at ambient temperature using a battery testing system (Neware BTS-2000). Finally, cyclic voltammogram and electrochemical impedance spectroscopy were carried out with a CHI660D electrochemical analyzer.

3. Results and discussion

3.1. Performance characteriazation of the $Fe_4(VO_4)_4 \cdot 5H_2O$ precursor

The TG-DTA curve of the $Fe_4(VO_4)_4 \cdot xH_2O$ compound is shown in Fig. 2. It can be seen that 11.5% mass lost in the temperature range from 25 °C to 410 °C in the TG curve and two endothermic peaks occurred at 120 °C and 340 °C in the DTA curve, indicating that the number of crystal water was five. Meanwhile, two exothermic peaks appeared in the DTA curve at 450 °C and 550 °C due to the decomposition of $Fe_4(VO_4)_4$ and the crystal transform, respectively. What's more, the Fe/V mole ratio of $Fe_4(VO_4)_4 \cdot xH_2O$ was 1.002 based on analysis of chemical titration, confirming that the prepared yellow precipitate was $Fe_4(VO_4)_4 \cdot 5H_2O$.

Fig. 3(a) shows the XRD patterns of $Fe_4(VO_4)_4 \cdot 5H_2O$. It can be seen the peaks were distributed widely and coarsely, demonstrating that the $Fe_4(VO_4)_4 \cdot 5H_2O$ was amorphous. As Fig. 5(b) shows, the obtained $Fe_4(VO_4)_4 \cdot 5H_2O$ was uniformly distributed and the average size of the particle was around 80 nm, obviously smaller than that reported in Ref. [13].

3.2. Physical performances of $2LiFePO_4 \cdot Li_3V_2(PO_4)_3/C$

Fig. 4(a) shows the XRD patterns of different $2LiFePO_4 \cdot Li_3V_2(PO_4)_3/C$ composites. It can be seen the composites were composed of orthorhombic $LiFePO_4$ (space group Pnmb, 200155-

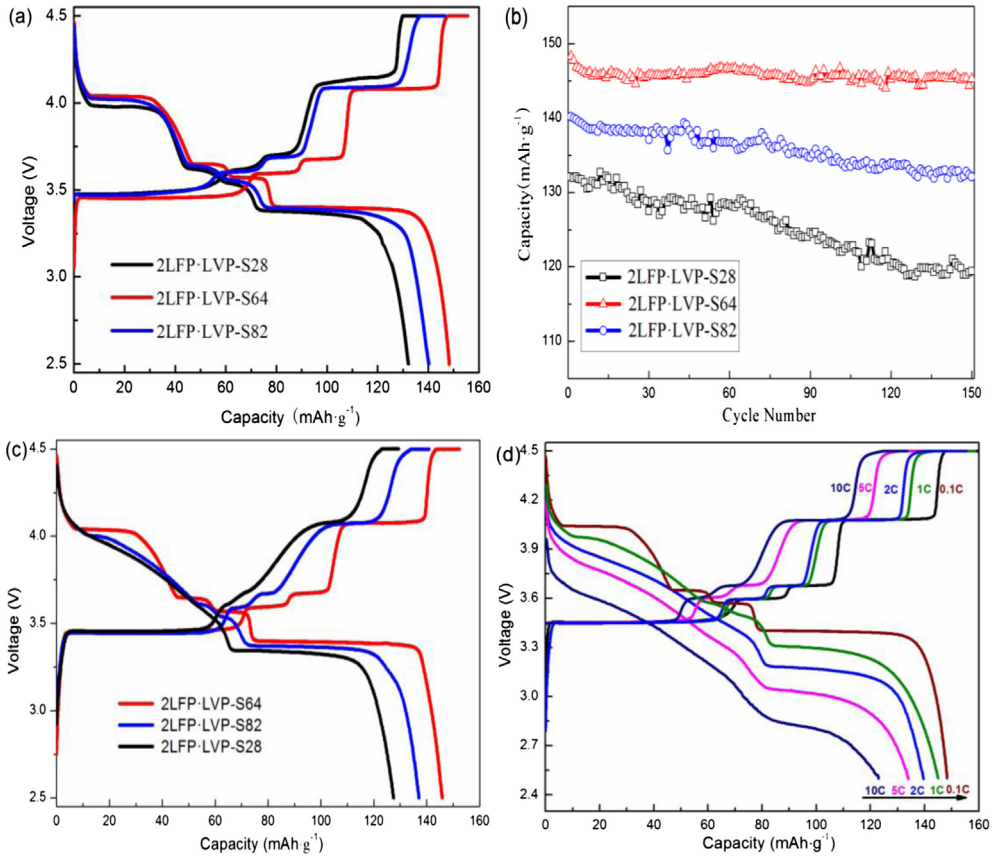

Fig. 8. (a) initial charge–discharge curves, (b) cycle performance and (c) charge–discharge curves after 150 cycles of different $2LiFePO_4 \cdot Li_3V_2(PO_4)_3/C$ composite at 0.1C, (d) rate performances of 2LFP·LVP-S64 composite.

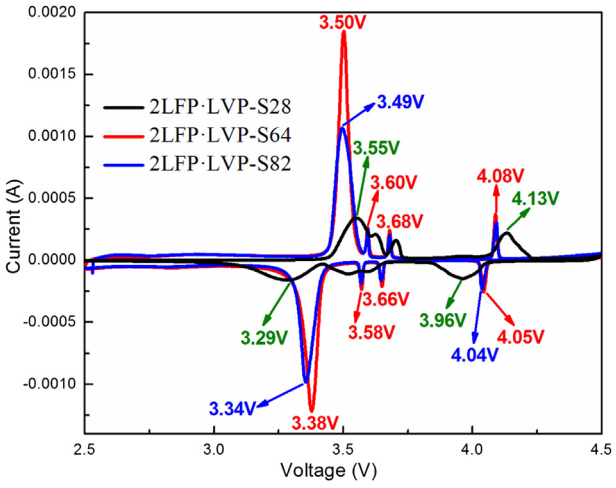

Fig. 9. Cyclic voltammetry profiles of the $2LiFePO_4 \cdot Li_3V_2(PO_4)_3$/C composite materials.

ICSD) and monoclinic $Li_3V_2(PO_4)_3$ (space group $P2_1/n$, 96962-ICSD) without any other impurities. There was no evidence of diffraction peaks for carbon in all samples. However, the content of carbon in 2LFP·LVP-S28, 2LFP·LVP-S64 and 2LFP·LVP-S82 samples were 1.02%, 2.05% and 2.98%, respectively by C—S analysis. It indicates the carbon is amorphous. Rietveld refinement was taken on these samples based on the two structural models, Pnmb and $P2_1/n$) by Maud 2.0 (see Fig. 4(b)). As seen Fig. 4(b), the weight ratio of $Li_3V_2(PO_4)_3$ is 57% and $LiFePO_4$ is 43%.

Fig. 5 shows the SEM images of the $2LiFePO_4 \cdot Li_3V_2(PO_4)_3$/C samples. The particles in all samples has a spherical morphology. From Fig. 5(a), (b), it can be seen the 2LFP•LVP-S28 particles had an irregular spherical morphology with numerous surface pores. Oxalic acid, acted as reductant and decomposed into CO_2 and H_2O ultimately, was oven-contained in the composite, thus the tap density of the composite was only 1.27 g cm^{-3}. With the increase of glucose content, the micro-particles morphology of 2LFP·LVP-S64 became regular gradually. Meanwhile, the particle size ranged from0.5 μm to 1.5 μm. The primary particles decrease obviously. Moreover, the sample shows a higher tap density (1.66 g cm^{-3}) and higher carbon content (2.05%) compared with 2LFP·LVP-S28 particles. It suggests that the glucose can restrain the growth of the

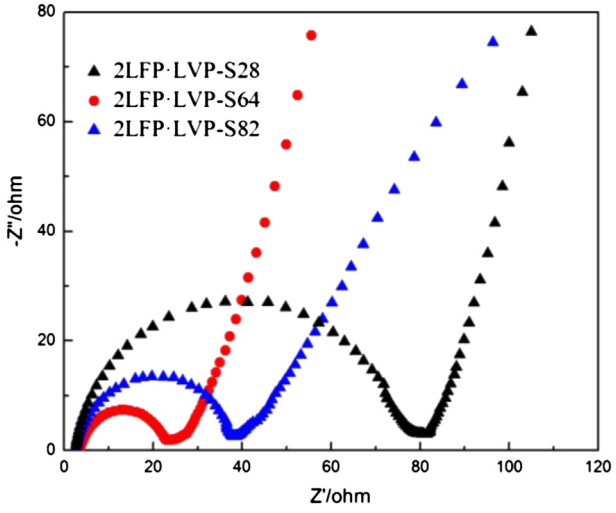

Fig. 10. Electrochemical impedance spectroscopy of the $2LiFePO_4 \cdot Li_3V_2(PO_4)_3$/C composite materials.

particles and decompose into pyrolytic carbon during the preparation process. However, when the amount of glucose continued increasing, the 2LFP·LVP-S82 particles formed aggregate. The carbon content in the composites was 2.98% carbon and the tap density was 1.42 g cm^{-3}. It can be concluded excessive glucose reduced the tap density due to particle agglomeration.

In order to investigate the distribution and the carbon coating information in the $2LiFePO_4 \cdot Li_3V_2(PO_4)_3$/C composites, SEM, EDS and HRTEM were employed in this paper. Fig. 6 exhibits the SEM images of 2LFP·LVP-S64 and the elemental mappings for C, O, P, V, and Fe. It can be seen each element was evenly distributed, indicating $LiFePO_4$, $Li_3V_2(PO_4)_3$ and carbon were well dispersed in the composites.

The HRTEM images of the 2LFP·LVP-S64 composites are shown in Fig. 7(a) and (b).It can be seen the prepared spherical particles have been coated by carbon uniformly. HRTEM was used to further study the microstructure of the as-prepared composites. Fig. 7(b) and (c) show the HRTEM images of the selected regions 1 and 2 in Fig. 7(a). The $2LiFePO_4 \cdot Li_3V_2(PO_4)_3$/C samples with the carbon thickness about 3 nm can be detected via the surface of the composites illustrated in Fig. 7(b).The coated carbon can form a conductive network among the particles to improve the electrical conductivity of the materials. Besides, the carbon film can inhibit the growth of the particles in the synthesis process. More information can be obtained from the TEM images, illustrated in Fig. 7(c). It shows that $2LiFePO_4 \cdot Li_3V_2(PO_4)_3$/C samples had a remarkable complicated microstructure. It is found that there were five lattice fringes of $LiFePO_4$ in the composites, with the interplanar spacing of 2.788 Å, 2.458 Å, 2.417 Å, 2.467 Å and 2.593 Å separately, corresponding to (3 0 1), (1 2 1), (4 1 0), (3 1 1) and (2 2 0) planes of $LiFePO_4$ (PDF #00-040-1499). The interplanar spacing of the other lattice fringes from $Li_3V_2(PO_4)_3$ were measured to be 2.702 Å, 2.396 Å, 2.202 Å, 2.622 Å and 2.992 Å, compatible with (1 4 1), (2 3 2), (3 2 2), (0 2 3) and (2 0 2) planes of $Li_3V_2(PO_4)_3$ (PDF #01-072-7074). The results imply that $LiFePO_4$ unit cell, $Li_3V_2(PO_4)_3$ unit cell and $LiFePO_4 \cdot Li_3V_2(PO_4)_3$ composite unit cell coexist in the composite materials. As shown in Fig. 7(c) and (f), the LVP and LFP particles were combined in the form of lattice with several nanometers. The above results further illustrate the existence of "mutual doping" between $LiFePO_4$ and $Li_3V_2(PO_4)_3$ phases. As shown in Fig. 7(d), (e) and (f), the compensatory TEM test result showed that the particles of the sample 2LFP-LVP-S28 are larger and the carbon layer is thiner(~2 nm) than that of 2LFP-LVP-S64. And seen from Fig. 7(f), for the sample 2LFP-LVP-S28, after 150 cycles, the particle lattice were still distinct, indicating that the fading did not arise from the collapse of the lattice but the bigger primary particle size and the thiner carbon layer.

3.3. *Electrochemical performance of $2LiFePO_4 \cdot Li_3V_2(PO_4)_3$/C*

Fig. 8(a) shows the first charge/discharge curves of the different $2LiFePO_4 \cdot Li_3V_2(PO_4)_3$/C samples at 0.1C rate. It can be seen four potential plateaus with 3.59 V, 3.67 V and 4.08 V for $Li_3V_2(PO_4)_3$ and 3.45 V for $LiFePO_4$. At 0.1C rate, 2LFP·LVP-S64 exhibited the optimal initial discharge capacity of 147.6 mAh g^{-1}, reaching 99.7% of the theoretical capacity of $LiFePO_4 \cdot Li_3V_2(PO_4)_3$ (The theoretic specific capacity (C_T) of $LiFePO_4 \cdot Li_3V_2(PO_4)_3$ is calculated with the following equation: $C_T = (170X_1 + 133X_2)$ (mAh g^{-1}), where 170 and 133 are the theoretic capacities of $LiFePO_4$ and $Li_3V_2(PO_4)_3$ (<4.5 V), respectively; X_1 and X_2 are the weight content of $LiFePO_4$ and $Li_3V_2(PO_4)_3$, respectively. Based on our Rietveld refinement results(Fig. 4(b)), the weight ratio of $Li_3V_2(PO_4)_3$ is 57%, so the C_T for $2LiFePO_4 \cdot Li_3V_2(PO_4)_3$/C synthesized in this paper is 148 mAh g^{-1}). The real capacity of the synthesized $LiFePO_4$ is about 73 mAh g^{-1}, and about 75 mAh g^{-1} for the $Li_3V_2(PO_4)_3$. While 2LFP·LVP-S28 and

2LFP·LVP-S82 are only 132.1 mAh g^{-1} and 140.2 mAh g^{-1}, respectively. It indicates the mass ratio of glucose/oxalic acid in the carbon sources had substantial effects on the electrochemical performances. In addition, the charge plateaus shifted downward and became wider with the increasing of glucose amount, whereas the discharge plateaus shifted upward, indicating that polarization between the charge and the discharge was somewhat suppressed by extra glucose.

The cycling performance of the different $2LiFePO_4 \cdot Li_3V_2(PO_4)_3$/C composites at 0.1C rate is shown in Fig. 8(b). It can be seen the 2LFP·LVP-S64 samples remained 98.4% of the initial cycle value (145.3 mAh g^{-1}) after 150 cycles at the rate of 0.1C, which was much higher than that for 2LFP·LVP-S28 (90.4%) and 2LFP·LVP-S82 (94.2%). The residual carbon content in 2LFP·LVP-S64 was 2.05%, which was adequate to form an effective carbon coating to provide decent conducting network for the kinetic extraction/insertion reaction of Li^+ ions [38,39]. It is noted that the capacity retention decreases with increasing additional glucose, so the capacity loss can be ascribed to the unconverted inactive 2LFP·LVP at the center of the particle or 2LFP·LVP of the trapped isolated zones too much for carbon in particles. Thus, the high-rate discharge performances of the 2LFP·LVP-S64 composites were investigated.

As shown in the Fig. 8(d), the discharge capacities of the composites at the rate of 0.1C, 1C, 2C, 5C and 10C were 147.6 mAh g^{-1}, 145.0 mAh g^{-1}, 141.0 mAh g^{-1}, 134.1 mAh g^{-1} and 123.0 mAh g^{-1}, respectively. The excellent electrochemical performance of the composites may be due to the homogeneous distribution, the proper ratio of co-carbon source and the micro-nano structure. With the proper mass ratio of glucose to oxalic acid, the composites have a conductive network among the particles to improve the electrical conductivity of the material. So the high electronic conductivity and the micro-nano LFP-LVP structure were advantageous to the rate capability and the cyclic performances of the composite materials.

The cyclic voltammetry curves of the different $2LiFePO_4 \cdot Li_3V_2(PO_4)_3$/C at a scan rate of 0.1 mV s^{-1} are presented in Fig. 9.It can be seen four redox couple peaks appear in the curves. The oxidation peak around 3.50 V and the reduction peak around 3.35 V belonged to the Fe^{2+}/Fe^{3+} redox potential for $LiFePO_4$, while the other three redox couple peaks should be the redox couple potential for $Li_3V_2(PO_4)_3$. Thus, the CV data were well consistent with the charge–discharge curves. Moreover, the potential differences between the anodic and cathodic peaks of 2LFP·LVP-S64 samples were smaller than others. The oxidation peak of 3.50 V and the reduction peak of 3.38 V belonged to the Fe^{2+}/Fe^{3+} redox potential for $LiFePO_4$, whereas the other three redox couple peaks associated with the V^{3+}/V^{4+} redox couple potential for $Li_3V_2(PO_4)_3$ were 3.60 V and 3.58 V, 3.68 V and 3.66 V, 4.08 V and 4.05 V. The results indicate that the electrochemical reversibility and the lithium ion diffusion of the $2LiFePO_4 \cdot Li_3V_2(PO_4)_3$/C composites were impressively improved by the proper mass ratio of glucose to oxalic acid for incorporation of $LiFePO_4$ and $Li_3V_2(PO_4)_3$.

Fig. 10 shows the electrochemical impedance spectroscopy of different $2LiFePO_4 \cdot Li_3V_2(PO_4)_3$/C composites after the first charge–discharge at rates of 0.1C. Each spectrum consisted of a semicircle in the high-frequency region and a straight line in the low-frequency region. The depressed semicircle in high-frequency region is attributed to the charge-transfer resistance (R_{ct}) of the electrochemical reaction while the straight line is related to the diffusion-controlled Warburg impedance [40].

As can be seen, the diameter of the depressed semicircle for the 2LFP·LVP-S64 composite was the smallest one among the samples, indicating that the charge-transfer resistance of 2LFP·LVP-S64 was much lower than that of others. In other word, this result also further confirms the good electrochemical performance of 2LFP·LVP-S64.

4. Conclusions

Micro-nano spherical $2LiFePO_4 \cdot Li_3V_2(PO_4)_3$/C composites were synthesized via spray drying method with the home-made $Fe_4(VO_4)_4 \cdot 5H_2O$ as precursor. $LiFePO_4$ and $Li_3V_2(PO_4)_3$ phases were well dispersed in the composite. The proper ratio of glucose to oxalic acid has predominant effects on the performances of the samples. The $2LiFePO_4 \cdot Li_3V_2(PO_4)_3$/C composite with the mass ratio of glucose to oxalic acid of 6:4 exhibited the excellent cycle performance and rate capability. The good electrochemical performance was attributed to the synergistic effect of the $2LiFePO_4 \cdot Li_3V_2(PO_4)_3$/C composite, as well as carbon coating.

Acknowledgment

This study was supported by National Natural Science Foundation of China (Grant No. 51302324 and 51272290), and the Technologies Program of Hunan Province in China (Grant No. 2010FJ6026).

References

[1] A.K. Padhi, K.S. Nanjundaswamy, J.B. Goodenough, J. Electrochem. Soc. 144 (1997) 1188–1194.
[2] B.L. Ellis, K.T. Lee, L.F. Nazar, Chem. Mater. 22 (2010) 691–714.
[3] S. Ferrari, R.L. Lavall, D. Capsoni, E. Quartarone, A. Magistris, P. Mustarelli, P. Canton, J. Phys. Chem. C 114 (2010) 12598–12603.
[4] H. Huang, S.C. Yin, T. Kerr, N. Taylor, L.F. Nazar, Adv. Mater. 14 (2002) 1525.
[5] S.C. Yin, H. Grondey, P. Strobel, H. Huang, L.F. Nazar, J. Am. Chem. Soc. 125 (2003) 326–327.
[6] G. Yang, H.D. Liu, H.M. Ji, Z.Z. Chen, X.F. Jiang, Electrochim. Acta 55 (2010) 2951–2957.
[7] F. Omenya, N.A. Chernova, S. Upreti, P.Y. Zavalij, K.W. Nam, X.Q. Yang, M.S. Whittingham, Chem. Mater. 23 (2011) 4733–4740.
[8] L.L. Zhang, G. Liang, A. Ignatov, M.C. Croft, X.Q. Xiong, I.M. Hung, Y.H. Huang, X.L. Hu, W.X. Zhang, Y.L. Peng, J. Phys. Chem. C 115 (2011) 13520–13527.
[9] M.R. Yang, W.H. Ke, S.H. Wu, J. Power Sources 165 (2007) 646–650.
[10] L.N. Wang, Z.C. Li, H.J. Xu, K.L. Zhang, J. Phys. Chem. C 112 (2008) 308–312.
[11] S.K. Zhong, L. Wu, J.Q. Liu, Electrochim. Acta 74 (2012) 8–15.
[12] Y. Guo, Y.D. Huang, D.Z. Jia, X.C. Wang, N. Sharma, Z.P. Guo, X.C. Tang, J. Power Sources 246 (2014) 912–917.
[13] J.C. Zheng, X.H. Li, Z.X. Wang, S.X. Niu, D.R. Liu, L. Wu, L.J. Li, J.H. Li, H.J. Guo, J. Power Sources 195 (2010) 2935–2938.
[14] H. Tang, X.D. Guo, B.H. Zhong, H. Liu, Y. Tang, R. Xu, L.Y. Li, J. Solid State Electrochem. 16 (2012) 1537–1543.
[15] J.C. Zheng, X.H. Li, Z.X. Wang, J.H. Li, L.J. Li, L. Wu, H.J. Guo, Ionics 15 (2009) 753–759.
[16] X.J. Chen, G.S. Cao, X.B. Zhao, J.P. Tu, T.J. Zhu, J. Alloys Compd. 463 (2008) 385–389.
[17] J.Y. Xiang, J.P. Tu, L. Zhang, X.L. Wang, Y. Zhou, Y.Q. Qiao, Y. Lu, J. Power Sources 195 (2010) 8331–8335.
[18] B. Zhang, J.C. Zheng, Z.H. Yang, Ionics 17 (2011) 859–862.
[19] S.K. Zhong, L. Wu, J.C. Zheng, J.Q. Liu, Powder Technol. 219 (2012) 45–48.
[20] J. Hong, X.L. Wang, Q. Wang, F. Omenya, N.A. Chernova, M.S. Whittingham, J. Graetz, J. Phys. Chem. C 116 (2012) 20787–20793.
[21] H. Lin, Y.W. Wen, C.X. Zhang, L.L. Zhang, Y.H. Huang, B. Shan, R. Chen, Solid State Commun. 152 (2012) 999–1003.
[22] X.P. Zhang, H.J. Guo, X.H. Li, Z.X. Wang, L. Wu, Solid State Ionics 212 (2012) 106–111.
[23] N. Hua, C.Y. Wang, X.Y. Kang, T. Wumair, Y. Han, J. Alloys Compd. 503 (2010) 204–208.
[24] G. Yang, C.Y. Jiang, X.M. He, J.R. Ying, F.P. Cai, Ionics 18 (2012) 59–64.
[25] J. Ma, B.H. Li, H.D. Du, C.J. Xu, F.Y. Kang, J. Electrochem. Soc. 158 (2011) A26–A32.
[26] C.S. Sun, Z. Zhou, Z.G. Xu, D.G. Wang, J.P. Wei, X.K. Bian, J. Yan, J. Power Sources 193 (2009) 841–845.
[27] M. Ren, Z. Zhou, Y.Z. Li, X.P. Gao, J. Yan, J. Power Sources 162 (2006) 1357–1362.
[28] J.F. Qian, M.Z. Zhou, Y.L. Cao, X.P. Ai, H.X. Yang, J. Phys. Chem. C 114 (2010) 3477–3482.
[29] H. Yang, X.L. Wu, M.H. Cao, Y.G. Guo, J. Phys. Chem. C 113 (2009) 3345–3351.
[30] Y.K. Sun, S.M. Oh, H.K. Park, B. Scrosati, Adv. Mater. 23 (2011) 5050–5054.
[31] M.M. Ren, Z. Zhou, X.P. Gao, W.X. Peng, J.P. Wei, J. Phys. Chem. C 112 (2008) 5689–5693.
[32] L. Wang, L.C. Zhang, I. Lieberwirth, H.W. Xu, C.H. Chen, Electrochem. Commun. 12 (2010) 52–55.
[33] L.J. Wang, X.C. Zhou, Y.L. Guo, J. Power Sources 195 (2010) 2844–2850.

[34] J.R. Ying, M. Lei, C.Y. Jiang, C.R. Wan, X.M. He, J.J. Li, L. Wang, J.G. Ren, J. Power Sources 158 (2006) 543–549.
[35] B. Zhao, Y. Jiang, H.J. Zhang, H.H. Tao, M.Y. Zhong, Z. Jiao, J. Power Sources 189 (2009) 462–466.
[36] T. Jiang, W.C. Pan, J. Wang, X.F. Bie, F. Du, Y.J. Wei, C.Z. Wang, G. Chen, Electrochim. Acta 55 (2010) 3864–3869.
[37] L.N. Wang, Z.G. Zhang, K.L. Zhang, J. Power Sources 167 (2007) 200–205.
[38] S.W. Oh, S.T. Myung, S.M. Oh, K.H. Oh, K. Amine, B. Scrosatiand, Y.K. Sun, Adv. Mater. 22 (2010) 4842–4845.
[39] L.L. Zhang, Y. Li, G. Peng, Z.H. Wang, J. Ma, W.X. Zhang, X.L. Hu, Y.H. Huang, J. Alloys Compd. 513 (2012) 414–419.
[40] F. Nobili, F. Croce, B. Scrosati, R. Marassi, Chem. Mater. 13 (2001) 1642–1646.